Poleward Transport of African Dust to the Iberian Peninsula Organized by a Barrier Jet and Hydraulic Jumps: Observations and High-Resolution Simulation Analyses

S. Dhital[a], M. L. Kaplan[a, b], J. A. G. Orza[c], and S. Fiedler[d]

[a]Division of Atmospheric Sciences, Desert Research Institute, 2215 Raggio Parkway, Reno, NV 89512, USA. sdhital@nevada.unr.edu

[b]Department of Applied Aviation Sciences, Embry-Riddle Aeronautical University, 3700 Willow Creek Road, Prescott, AZ 86301, USA. kaplanm1@erau.edu

[c]SCOLAb, Department of Applied Physics, Universidad Miguel Hernández de Elche, Av. de la Universidad s/n, 03202 Elche, Spain. ja.garcia@umh.es

[d]Institute of Geophysics and Meteorology, University of Cologne, Pohligstr. 3, 50969 Köln, Germany. stephanie.fiedler@uni-koeln.de

Corresponding author: Saroj Dhital (sdhital@nevada.unr.edu)

Saroj Dhital

Division of Atmospheric Sciences

Desert Research Institute

2215 Raggio Parkway

Reno, NV, 89512, USA

Tel. +1 7753797818

Highlights:

- Saharan dust episode with a strong impact poleward over the Iberian Peninsula.
- High-resolution WRF-Chem simulations of a severe African dust storm.
- Multi-scale terrain-induced circulations are instrumental for dust ablation.
- Barrier jet and hydraulic jumps organize dust storms.
- Hydraulic jumps are linked to a mesoscale gravity wave.

Abstract

Most air quality stations in Spain exceeded the European Union's daily PM_{10} limit due to the February 2016 Saharan dust outbreak, which resulted from two successive dust storms in Northwest Africa. This study identifies the meso-β/meso-γ-scale dynamical processes responsible for developing these dust storms using observations and high-resolution Weather Research and Forecasting model coupled with Chemistry simulations. The results revealed that the first dust storm was associated with a strong barrier jet (BJ). The BJ formed on the southeastern foothills of the Saharan Atlas Mountains (SAM) when an easterly-northeasterly low-level Mediterranean flow was blocked by a stably stratified layer close to the SAM. The BJ intensified just after sunrise on 20 February and the associated near-surface peak winds organized the first dust storm. The second dust storm was linked to a mesoscale gravity wave (MGW) and hydraulic jumps. A long-lived westward propagating MGW was triggered by a downslope flow interacting with the stable layer near the northeastern edge of the Tinrhert Plateau in eastern Algeria. When this MGW crossed the Tademaït Plateau, hydraulic jumps formed on its lee side. The strong winds accompanying these hydraulic jumps formed the second dust storm on 21 February. The lifted dust extended over a depth of 2-3 km in the growing daytime boundary layer and was advected poleward by the southerly/southeasterly mid-tropospheric winds. Our results underline the importance of resolving terrain-induced mesoscale processes to understand dust storm dynamics, which are difficult to represent in coarse-resolution numerical models.

Keywords: Saharan dust storm, terrain-induced circulations, barrier jet, hydraulic jumps, WRF-Chem

1 Introduction

Terrain-induced meso-β/meso-γ-scale meteorological features are known to organize severe dust storms over North Africa. Known mechanisms include downslope winds associated with hydraulic jumps (e.g., Gläser et al., 2012; Pokharel et al., 2017), convectively generated density currents linked through orographic forcing (Knippertz et al., 2007; Roberts & Knippertz, 2014), and density current-like cold fronts and undular bores (e.g., Dhital et al., 2020). A regional model simulation by Gläser et al. (2012) identified strong near-surface winds accompanying a hydraulic jump on the southern slope of the SAM that emitted dust during the early stage of the March 2004 Saharan dust outbreak. Similarly, Pokharel et al. (2017) showed that downslope windstorms and hydraulic jumps on the southern slope of the SAM and southwestern slopes of the Tibesti Mountains in Chad occurred as a small-scale and isolated precursor wind event before the formation of a large-scale dust storm. Dhital et al. (2020) found that a density current-like cold front induced an undular bore that organized the 10-13 November 2017 strong dust episode on the southern flank of the SAM, which ultimately impacted the Cape Verde Islands. The study by Roberts and Knippertz (2014) on the June 2010 intense Haboob near the Hoggar and Aïr Mountains found that a terrain forcing mechanism favored the formation of convective cold pools and associated strong winds critical for dust emission. Knippertz et al. (2007) suggested that instability paired with a relatively high moisture content over the Saharan Atlas triggered deep moist convection and an associated dust-emitting density current.

Another phenomenon of potential interest in complex terrain is the barrier jet (BJ), which represents a class of strong low-level mesoscale winds that develop adjacent to steep terrain (e.g., Parish 1982). A BJ forms when the low-level upstream flow is blocked (e.g., Loescher et al., 2006). This requires a low-level stable stratification that enhances the pressure gradient force parallel to the windward side of a mountain barrier. In response, the flow is accelerated and redirected parallel to the mountain barrier. Given the necessary stable stratification, BJs are frequent during the cool season (e.g., Colle et al., 2006; Neiman et al., 2010). They have, for instance, been observed over the Appalachian Mountains (e.g., Bell and Bosart 1988), in the Colorado Rockies (e.g., Cox et al., 2005), the western slope of the Sierra Nevada Mountains (e.g., Parish 1982; Neiman et al., 2010), the Pacific Northwest (e.g., Braun et al. 1997), the Alaskan coast (e.g., Loescher et al., 2006, Colle et al., 2006;), the Gulf of Mexico (Luna-Niño & Cavazos, 2018), and Taiwan (Li and Chen, 1998).

Another ubiquitous feature in complex terrain is the hydraulic jump which forms in conjunction with downslope winds on the lee side of a mountain barrier when an upstream flow has enough kinetic energy to overcome the potential energy associated with a mountain barrier. Besides North Africa, downslope winds and hydraulic jumps have been observed over the eastern Sierra Nevada and Owens Valley, California (Lin, Y., 2007), the front range of the Rocky Mountains (Karyampudi et al., 1995), northern Australia (e.g., Clark, 1972), and the Middle East (e.g., Pokharel et al., 2017).

The dimensionless Froude number, $Fr = U/(Nh)$, has been frequently used to characterize the upstream flow regime (e.g., Kaplan et al., 2012; Pokharel et al., 2017), where U is the ambient wind speed perpendicular to the mountain barrier, N is the Brunt-Väisälä frequency, and h is the barrier height. An upstream subcritical flow ($Fr<1$) favors BJ formation, while supercritical flow ($Fr>1$) favors hydraulic jumps and associated downslope wind formation. In the hydraulic jump region, the flow changes from a supercritical regime to a subcritical regime.

Severe weather related to BJs and hydraulic jumps have been documented in previous studies. For example, Neiman et al. (2013) showed that an interaction between the Sierra barrier jet, i.e., the BJ on the western side of the Sierra Nevada Mountain range, and an atmospheric river resulted in heavy precipitation and flooding events in the Central Valley of California. Ke et al. (2019) identified that the interaction between a BJ and a cold pool outflow associated with mesoscale convection results in strong convection and heavy precipitation over northern Taiwan during the Mei-Yu season, i.e, mid-May to mid-June. Similarly, outside North Africa, the importance of hydraulic jumps and an undular bore in a severe weather outbreak has also been highlighted. Karyampudi et al. (1995), in their study of the April 1986 severe weather outbreak over eastern Colorado and western Nebraska, identified the formation of a downslope windstorm associated with a hydraulic jump and undular bore to the east of the Rockies when a density-current like cold front spilled onto the lee side of the mountains. The interaction between a downstream propagating undular bore, lee cyclone, a dryline, and a warm front triggered deep convection as well as intense blowing dust in this case.

A severe African dust outbreak over the IP occurred during 20-21 February 2016. Dust plumes were swept by zonal flows eastwards on subsequent days and eventually impacted Germany (https://www.dlr.de/eoc/en/desktopdefault.aspx/tabid-11128/19488_read-45631/). A detailed ground-based observational analysis on this outbreak by Titos et al. (2017) found that ~90 % of the air quality stations in Spain exceeded the European Union's daily PM_{10} limit of 50 $\mu g.m^{-3}$. Gama et al. (2019) also highlighted the severity of this dust outbreak over Portugal on air quality based on observational and modeling studies. However, this study did not focus on the detailed analysis of the dust emission processes. In a companion paper (Orza et al., 2020; hereafter referred to as Part I), the synoptic analysis of this dust episode was presented in detail. During this episode, two distinct dust plumes reached the IP in succession-the first of two dust plumes crossed the SAM during midday on 20 February and was advected towards the Western IP. The second one followed in the afternoon of 21 February and was advected towards the Eastern IP. Part I highlighted a double Rossby Wave Break (RWB) in the polar jet stream (PJ) linked through nonlinear wave reflection as an upper-level synoptic precursor flow that favored this dust storm formation and subsequent poleward transport of dust to the IP.

In this paper, we extend our analyses to meso-β/meso-γ-scale meteorological processes and highlight the importance of a BJ and hydraulic jumps in organizing this dust outbreak to Europe. We find that the BJ is another important terrain-induced mechanism for severe dust outbreaks. The BJ results in strong near-surface winds capable of emitting dust from potential source regions on the windward side of a mountain barrier. For perhaps the first time for the entire of North Africa, this study documents a BJ and assesses the role in organizing a strong dust storm. In addition to the BJ, this study also provides evidence of a subsequently occurring severe dust storm organized by hydraulic jumps in association with a long-lived mesoscale gravity wave (MGW). MGWs are gravity waves, with a wavelength longer than 50 km and periods exceeding 1 hr (Ruppert and Bosart, 2014), which have been known for their role in different severe weather events (e.g., Uccellini and Koch, 1987; Kaplan et al., 1997), but not for North African dust storms.

The remainder of this paper is organized as follows. Section 2 provides an overview of our data, methods, and model configuration. The synoptic setup for BJ, mesoscale wave dynamics, and observational analysis of the spatiotemporal evolution of the dust storm is presented in Section 3. Section 4 outlines the detailed dynamics of the BJ and hydraulic jumps, highlighting their importance in this dust storm occurrence. The summary and conclusions of the present study are presented in Section 5.

2 Data and methods

2.1 Observations

Wind speed, wind direction, and visibility data for the observational network distributed over the study area (Figure 2a), for 20-21 February 2016, were obtained from the Meteorological Terminal Aviation Routine Weather Report (https://mesonet.agron.iastate.edu/request/download.phtml) and provided the time and location of the reduced visibility associated with this dust storm. The combined Dark Target Deep Blue aerosol optical depth (τ) from the Moderate Resolution Imaging Spectroradiometer aboard the Aqua satellite (https://ladsweb.modaps.eosdis.nasa.gov/) and sounding data from the University of Wyoming (http://weather.uwyo.edu/upperair/sounding.html) provided the spatial extent of the dust evolution and vertical profiles for the model validation. The large-scale flow features that create a favorable environment for BJ formation were described using the European Center for Medium-Range Weather Forecast (ECMWF) ERA-Interim reanalysis dataset (Dee et al., 2011). We used the charts of potential vorticity (PV) and horizontal wind at the 330 K isentropic surface and 850 hPa temperature and wind.

2.2 Model configuration

Meso-β-/meso-γ-scale meteorological processes are analyzed in high-resolution simulations with a one-way nesting approach using the WRF-Chem model version 3.9 (Grell et al., 2005). The outer, middle, and inner domain's horizontal resolutions are 18, 6, and 2 km, respectively, and covered the area as shown in Figure 2a. All the model simulations have 40 vertical levels, with higher resolution in the lower atmosphere and the vertical boundary condition at 50 hPa. The parent domain is initialized using the ERA-Interim reanalysis data, while the inner nested domains are initialized by the simulation results from the outer domain. The outer, middle, and inner domains are initialized at 00 UTC, 06 UTC, and 12 UTC on 19 February, respectively, and all end at 06 UTC on 21 February.

In this study, the convective parameterization is employed in the 18 km simulation only using the Betts-Miller-Janjic scheme (Janjic, 1994) and turned off in the high-resolution domains (6 and 2 km) thus explicitly resolving moist convection on the model grid. Our model configurations are otherwise identical across the different resolutions. The model configuration uses the double-moment bulk microphysical parameterization (Thompson et al., 2008), the Mellor-Yamada-Janjic (MYJ) PBL scheme (Mellor & Yamada, 1974; Janjic, 2002), Noah Land Surface Model (Chen & Dudhia, 2001; Ek et al., 2003), the Dudhia shortwave radiation scheme (Dudhia, 1989), and the RRTM for longwave radiation (Mlawer et al., 1997). These parameterizations have been successfully used to simulate several terrain-induced mesoscale meteorological features organizing strong dust storms over North Africa (e.g., Pokharel et al., 2017; Dhital et al., 2020).

The WRF-Chem simulation is performed in dust-only mode following the Georgia Tech/Goddard Chemistry Aerosol Radiation and Transport (GOCART) dust scheme (Ginoux et al., 2001). The GOCART scheme includes five dust bins having effective radii of 0.73, 1.4, 2.4, 4.5, and 8 μm. The model outputs dust τ at 550 nm using the corresponding columnar mass load and the extinction efficiencies at 550 nm and dust concentration in each size bin. The simulated dust emission flux (F_p) in the GOCART dust scheme is a function of wind speed, erodibility, and surface wetness and is calculated using equation (1).

$$F_p = CSs_p u_{10m}^2 (u_{10m} - u_t) \quad \text{if } u_{10m} > u_t \qquad (1)$$

where the constant $C = 1\ \mu g.m^{-5}.s^2$, S is source function, s_p is the mass fraction of size group p of dust emission, u_{10m} is the wind at 10m height, and u_t is the threshold wind velocity for the effects of wind erosion. The source function (S) is a dimensionless quantity, which depends upon the soil properties. The meteorological interpretations are made based on 2 km simulation outputs unless otherwise stated.

3 Observed downscale evolution from RWB to mesoscale dust plumes

3.1 Synoptic setup for barrier jet and mesoscale wave dynamics

Figure 1 depicts the 330K winds and isentropic PV as well as the 850 hPa temperatures and wind vectors during the precursor period from 00 UTC 19-20 February. In this period, the favorable thermodynamic profile for the BJ develops above the Atlas Mountains. The 330K fields indicate an anticyclonic RWB in the PJ above the western European Coast extending offshore and south southwestward. This feature subsequently propagates southeastward towards the northwestern African Coast during this 24-hour period (Figures 1a, c, and e). The RWB and PV reversal is the result of a tongue of PV wrapping anticyclonically into northwestern Africa and is in proximity to the subtropical jet stream (STJ) exhibiting substantial southwesterly flow. This southwesterly flow creates a strong confluence and shearing deformation zone from the tropopause to the lower troposphere over northwestern Africa. At the same time, one sees the intensifying low-level baroclinic zone at 850 hPa and that surface's confluent wind vectors centered near the SAM (Figures 1b, 1d, and 1f). This baroclinic zone is the result of the frontogenesis in the aforementioned confluence/shear zone in the low-middle troposphere as: 1) polar air over northern Europe is advected south-southwestward within the RWB in proximity to 2) hot continental tropical (CT) air above the Sahara Desert being advected towards and over the Atlas Mountains. This deep frontogenetical zone, where north-northeasterly low-level flow caused by the PJ RWB and the low-level south-southwesterly return branch jet in the STJ converge, is critical for setting up the BJ. The favorable conditions for the BJ are established as the very warm CT air under the STJ overruns cooler Mediterranean air emanating from the north-northeast under the PJ thus resulting in the statically stable and veering flow described earlier above the Atlas Mountains which is so conducive to blocking and BJ formation. The large magnitude static stability results from the intensifying frontogenetical circulation accompanying the overrunning of CT air on the equatorward slope of the Atlas Mountains in Algeria and Morocco. The hot, dry CT air plume originating as part of the low-level return branch in the 700-850 hPa layer under the STJ from the western Sahara.

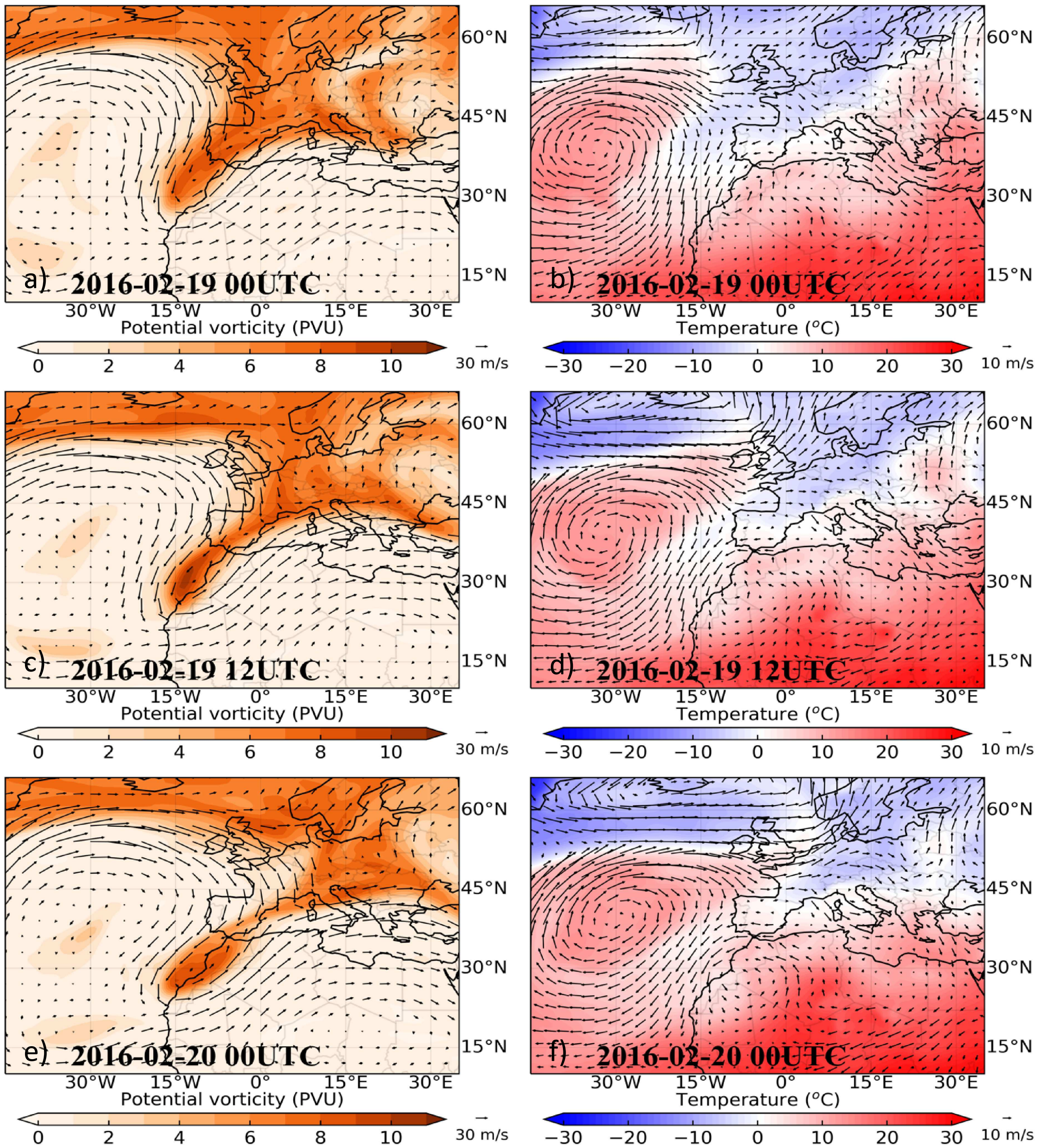

Figure 1. PV and wind vector at the 330 K isentropic surface (left). Temperature and wind vector at the 850 hPa level (right). (a, b) at 00 UTC, (c, d) at 12 UTC on 19 February, and (e, f) at 00 UTC on 20 February.

3.2 Spatiotemporal evolution of the observed dust outbreak

Our observational analyses suggest that this dust episode was associated with two successive dust storms initiated on the southeastern side of the SAM. The first dust storm started ~09 UTC on 20 February and second storm began ~01 UTC on 21 February. The lifted dust then ultimately was advected poleward towards the IP (see Figure 3 in Part I). Figure 2 illustrates the observed wind speed, wind direction and visibility for 20-21 February 2016 at different stations in Algeria. The initial signal of the dust storm was recorded at two stations [Tilrempt (DAFH, 32.93°N, 3.31°E) in Laghouat Province and Béchar (DAOR, 31.62°N, 2.23°W) in Béchar Province] at 08 UTC on 20 February (Figures 2b and 2d). The DAFH station recorded an easterly wind speed of 10.29 $m.s^{-1}$ and visibility of 4.97 km, while the DAOR station recorded an east-southeasterly wind speed of 11.3 $m.s^{-1}$ and visibility of 1.24 km. At 09 UTC, the DAFH station recorded an east-southeasterly wind speed of 11.3 $m.s^{-1}$ and visibility of 2.49 km while the Ghardaia station (DAUG, 32.38°N, 3.79°E) in Ghardaïa Province recorded a northeasterly wind speed of 14.4 $m.s^{-1}$ and visibility of 4.97 km (Figures 2b and 2c). The visibility was unchanged at the DAOR station with an easterly wind speed of 10.29 $m.s^{-1}$. At 10 UTC, the wind speed at three stations (DAFH, DAUG, and DAOR) further increased and the visibility remained <3 km. At 11 UTC, a significant reduction in visibility was observed at the Mecheria station (DAAY, 33.58°N, 0.28°W) in Naâma Province in the Atlas Mountains which recorded an easterly/southeasterly wind speed of 12.34 $m.s^{-1}$ and visibility of 1.98 km (Figure 2f), pointing to the occurrence of desert-dust aerosols. Concurrently, the El Bayadh station (DAOY, 33.67°N, 1°E) in El Bayadh Province reported a dust storm associated with a southeasterly wind speed of 11 $m.s^{-1}$ and visibility of 3.11 km (Figure 2e). The visibility at the DAFH, DAUG, and DAOR stations remained <5 km for the 12-18 UTC period. A continuous reduction in visibility was observed at the DAOY (<3km) and DAAY (<2.5km) stations with a southeasterly wind speed of >9 $m.s^{-1}$ until 15 UTC on 21 February. Additionally, starting 03 UTC on 21 February, the visibility at the DAOR station again started to decrease and remained <3 km till 14 UTC.

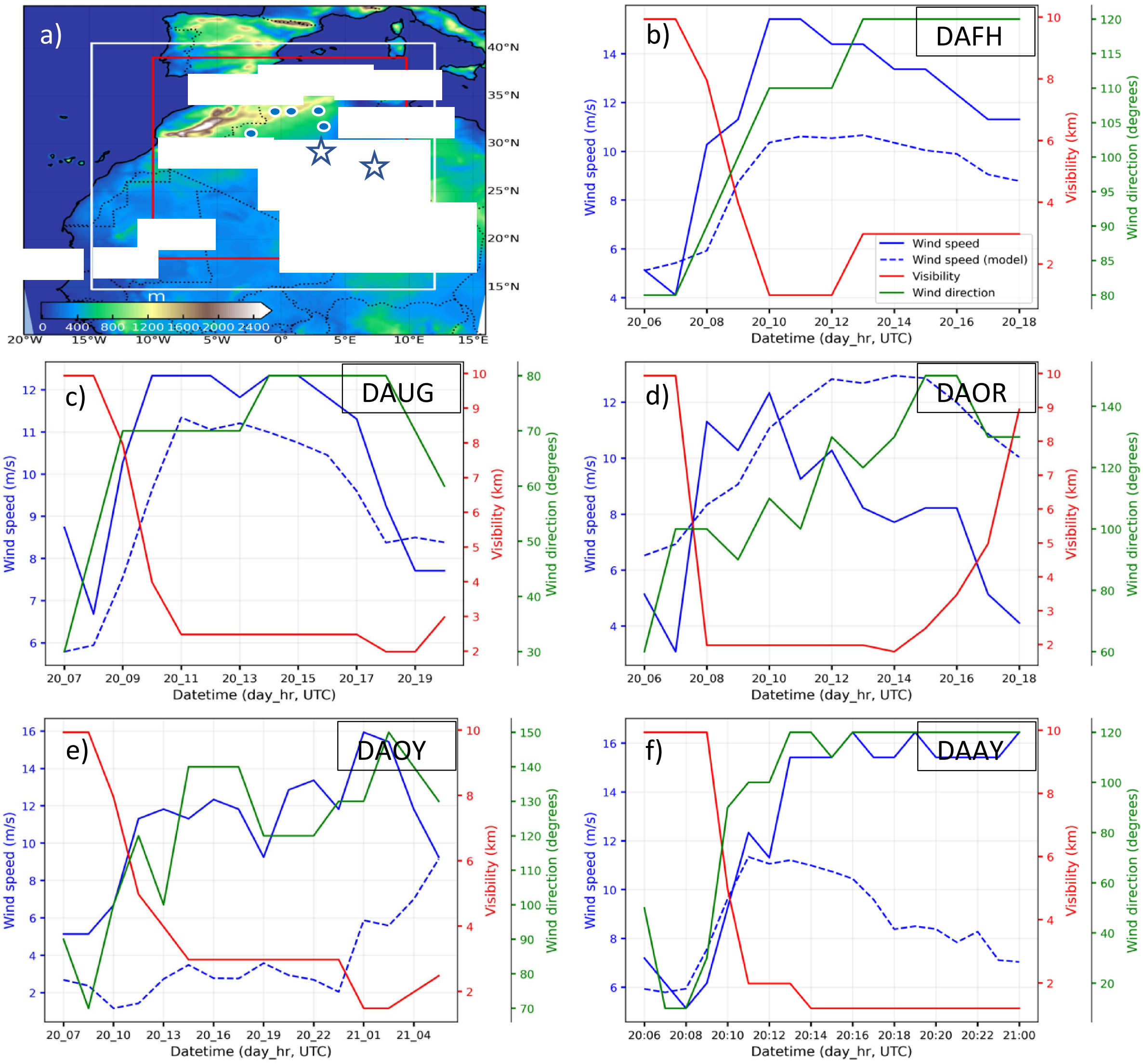

Figure 2: (a) WRF-Chem simulation domain, where d1, d2, and d3 represent the domains of 18, 6, and 2 km horizontal resolution, respectively. Time series of wind speed, visibility, and wind direction are shown for the stations in (b) DAFH, (c) DAUG, (d) DAOR, (e) DAOY, and (f) DAAY. The dots indicate the locations of the available hourly meteorological stations and stars mark the center of plateaus mentioned in the text. TP is an abbreviation for the Tademaït Plateau.

4 High-resolution simulation results

4.1 Model validation with observations

The simulated dust τ qualitatively reproduces the observed dust plume. A thick dust plume, as indicated by the higher values of simulated τ >0.5, was present over the Atlas Mountains (blue box in Figure 3a), consistent with the reduced visibility at the DAOR station ~13 UTC on 20 February. After 15 min, the MODIS-Aqua overpass at 1315 UTC also captured the τ >0.5 over the same region (blue box in Figure 3b). The observed τ was higher over the

Atlas Mountains range outside of the marked region and suggests an underestimation of the simulated dust τ over the ocean regions to the North. The observations, however, include all aerosol species. An underestimation of dust τ in the model compared to total τ in the observations is, therefore, to be expected. For instance, the simulated dust τ does not account for the anthropogenic aerosols and sea-salt aerosols. The τ pattern from MODIS is due to clouds (see Figure 3 in Part I).

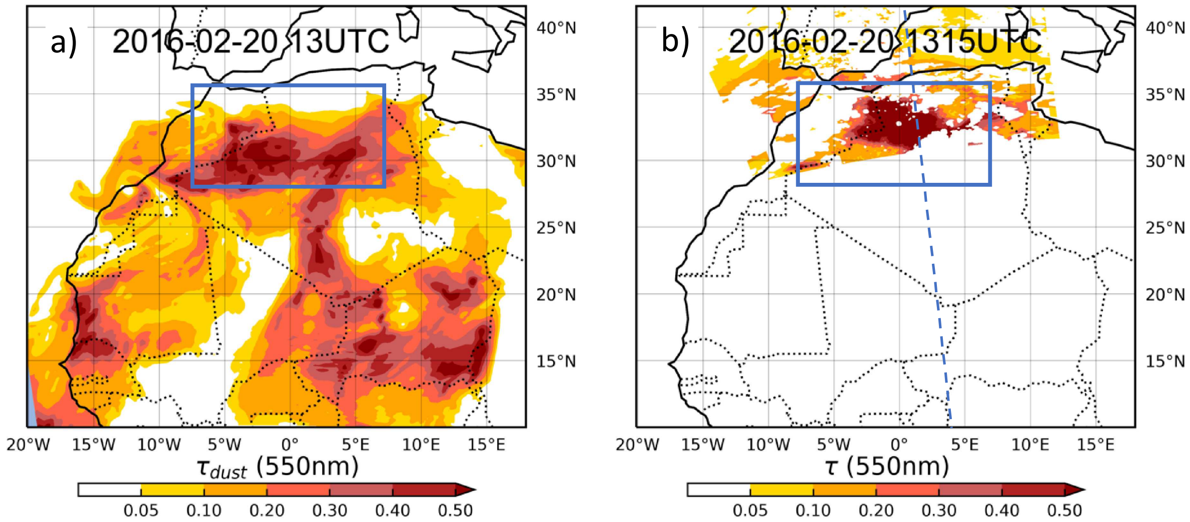

Figure 3: Aerosol optical depth. Shown are the (a) WRF-Chem simulated (18 km) dust τ at 13 UTC on 20 February 2016 and the (b) Dark Target Deep Blue combined τ at 550 nm from the MODIS aboard Aqua at 1315 UTC 20 February 2016. The dashed blue line represents the MODIS Aqua overpass. The blue boxes mark the τ over the Atlas Mountains discussed in the text.

The comparison between observed and simulated 10m wind speed at three stations, namely DAFH, DAUG, and DAOR, shows that the simulated wind speed generally followed the observed wind pattern (Figures 1b-d). At 09-10 UTC February 20, when BJ formed, and visibility started to decrease, the observed wind speed was ~10-15 $m.s^{-1}$, and the simulated wind speed was ~8-11 $m.s^{-1}$, suggesting an underestimation of simulated wind speed. During 10-16 UTC, the simulated wind speed at the DAFH and DAUG was between 10-11.5 $m.s^{-1}$, while the observed wind speed ranged between 11.5-15 $m.s^{-1}$(Figure 1b-c). However, at the DAOR station, the simulated wind speed remained between 11-13 $m.s^{-1}$and the observed wind speed ranged between 8-12 $m.s^{-1}$ (Figure 1d), suggesting an overestimation of the simulated wind speed. Over the Saharan Atlas region, at the DAAY station, the simulated wind speed closely matches with the observation during 09-12 UTC(Figure 1e). At a later time, the simulated wind speed does not follow the observed wind speed pattern at the same station and at the DAOY station(Figure 1e-f). The models' inability to generate a similar wind evolution at these two stations is probably because the model could not capture small-scale features over the Saharan Atlas Mountains complex topography. To summarize, the evolution of the simulated wind speed on the southern flank of the Atlas Mountain, where the dust storm was formed, generally followed the observation with sufficient magnitude to emit dust from the source region providing confidence in our simulation to assess the dynamics of dust storm formation.

Additionally, the observed and simulated temperature and wind profiles at the Béchar radiosonde station in Algeria at 00 UTC on 20 February are in close agreement (Figures 4a-b).

One can notice the presence of (1) a near surface stable layer, (2) vertically veering flow with a secondary elevated inversion layer, and (3) sharp changes in winds in both soundings. However, differences also exist between simulated and observed soundings. Near the surface, the simulated air temperature is ~8°C, and the observed temperature is ~12°C. At ~ 900 hPa, the simulated and observed air temperatures are ~10°C and ~11°C, respectively. Also, ~650 hPa level, the observed and simulated dew point depressions are ~35°C and ~23°C, respectively, which indicates a more dry layer in the observation than in the simulation. Still, both soundings show a similar pattern of the near-surface stable layer and the vertical wind profiles necessary to make a favorable environment for BJ formation. The good agreement with the observations indicates that the complex vertical atmospheric structure, important for the mesoscale process analysis, is reproduced by our simulation.

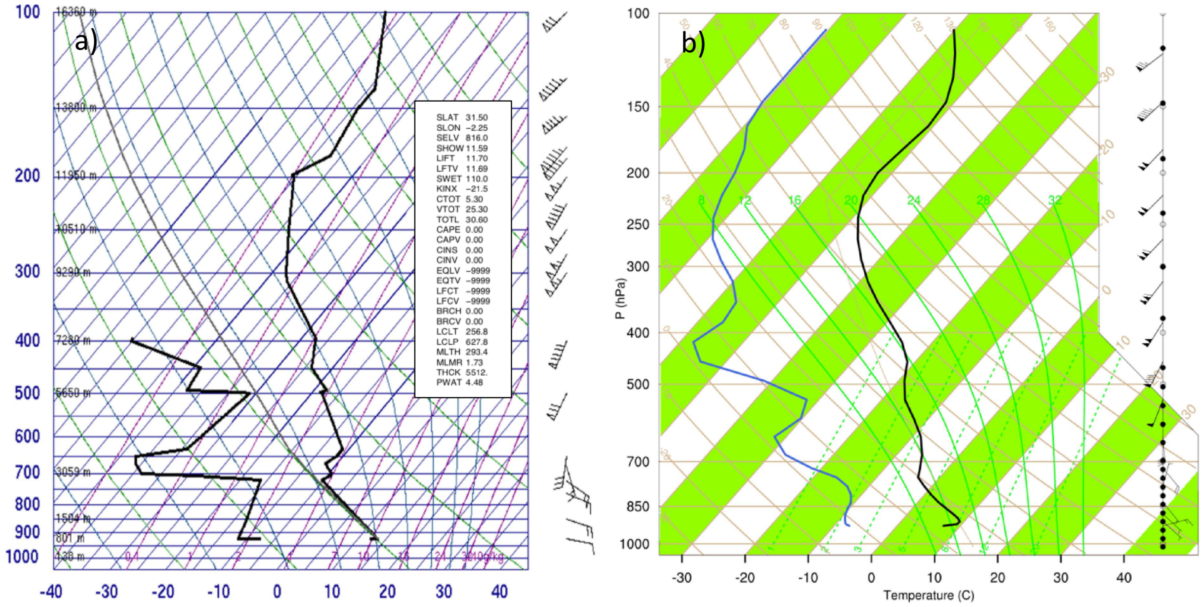

Figure 4: Skew T-Log P diagram at the Béchar station at 00 UTC on 20 February 2016 from the (a) observed sounding and (b) WRF-Chem simulation.

4.2 Simulated dust evolution

The evolution of the dust outbreak is analyzed using the horizontal winds and dust load at different atmospheric levels. At 09 UTC on 20 February, winds exceeding 25 $m.s^{-1}$ were observed over the ~30-32°N, 0-2°E region (Figure 5a). On the southeastern foothills of the SAM, the wind speed was >15 $m.s^{-1}$. These strong winds emitted dust aerosols (Figure 6a and 7a) and formed the first dust storm. Concurrently, dust loading on the southeastern foothills of the SAM was ~0.5 $g.m^{-2}$.

Different wind directions are observed at different heights, suggesting the advection of lifted dust towards different height-dependent directions. At the 850 hPa level, the southeasterly flow turned to easterly when it reached the windward side of the Atlas range and the flow became stronger near Béchar Province (Figure 5c). However, at the 700 hPa level, which is above the mountain top, the southerly/southeasterly flow prevailed in the region (Figure 5e).

Here, the emitted dust was mostly advected downwind of the Béchar station because of the predominantly low-level northeasterly flow (Figures 5a and 5c).

The freshly emitted dust did not reach high altitudes initially such that no significant poleward advection by mid-tropospheric winds occurred at this stage (Figures 5e, 6a, and 7a), due to the near-surface stable layer in the morning. At 12 UTC, noticeable features were observed in the wind field at different atmospheric levels. The strength of the near-surface wind decreased (Figure 5b), but the wind speed at higher atmospheric levels and the dust load increased. This indicates upward mixing of the dust by midday when the daytime heating had eroded the surface inversion and dry convection mixed the dust upward. Both the 850 and 700 hPa winds strengthened over Béchar Province. However, the wind fields were different: east-south-easterly at 850 hPa and southerly at 700 hPa (Figures 5d and 5e). A significant amount of dust started to advect poleward with an increasing dust load over Béchar Province (see rectangular box in Figure 6b). The dust loading over the top of the SAM was >0.5 $g.m^{-2}$ consistent with the strengthening of 700 hPa southerly/southeasterly wind (Figures 5f and 6b). These mid-tropospheric winds advected the dust poleward.

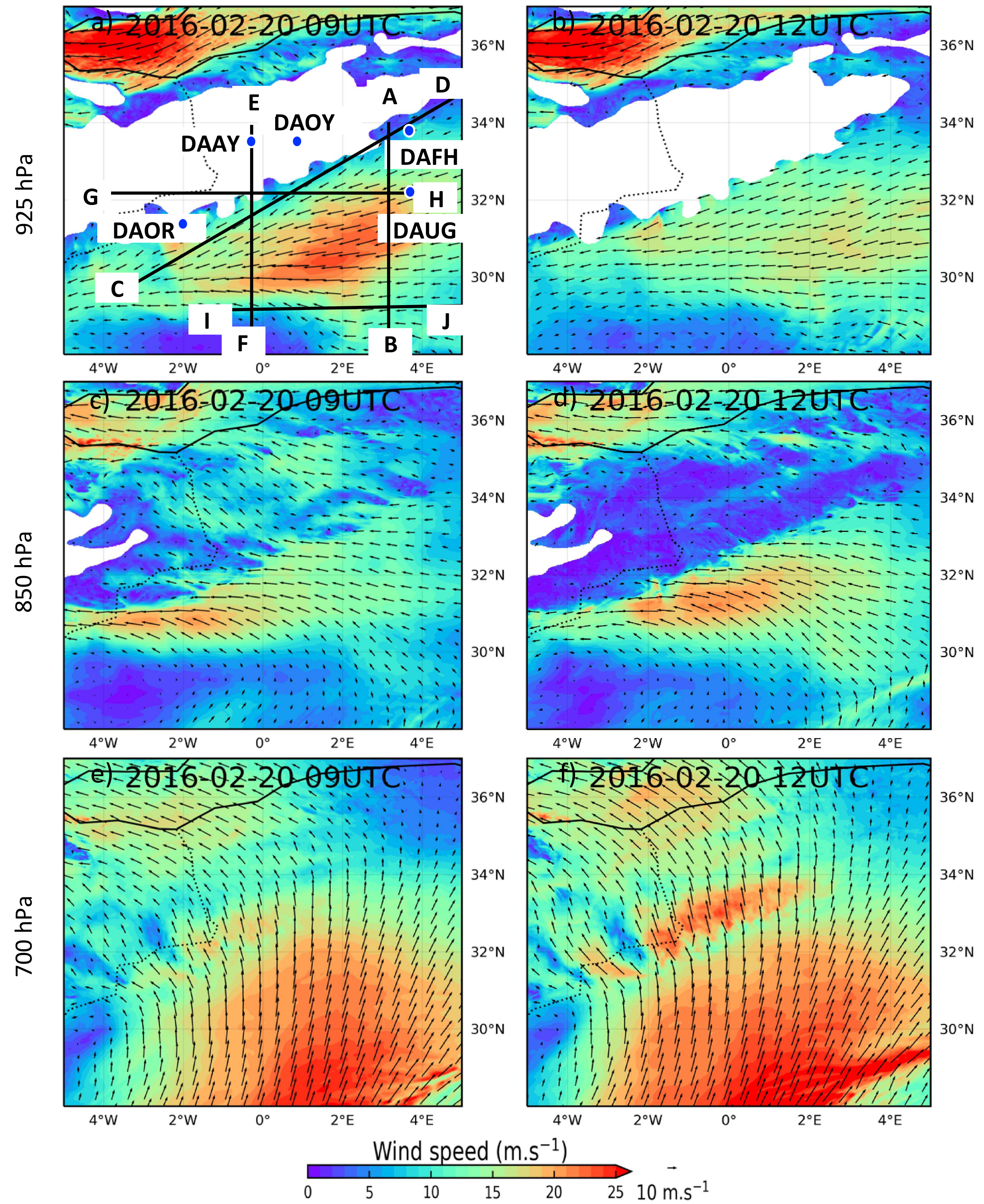

Figure 5: WRF-Chem simulated horizontal wind vector and speed (fill in m.s^{-1}) at (a, b) 925 hPa, (c, d) 850 hPa, and (e, f) 700 hPa and valid for 09 UTC (left) and 12 UTC (right) on 20 February 2016. The solid black lines mark cross-sections used in later analyses: A-B (28°N, 3°E to 34°N, 3°E), C-D (30°N, 3.5°W to 34.5°N, 5°E), E-F (28°N, 0.28°W to 34°N, 0.28°W), G-H (32.38°N,

4°W to 32.38°N, 4°E), I-J (29°N, 1°W to 29°N, 7°E). The white area represents elevation above the pressure levels.

At the beginning of the second dust storm, the dust load started to increase on the western side of the TP. At ~18 UTC on 20 February, the 10m wind suddenly began to increase on the west side of the TP, which emitted dust aerosol (black circle in Figure 6c). Synchronously, dust loading again started to increase near Béchar Province, where the dust load reached >3.5 $g.m^{-2}$. The 10m wind further strengthened on the lee side of the TP by 01 UTC on 21 February resulting in the second strong dust storm (solid black line in Figure 6d). Afterward, a dust front, or first-order discontinuity in the concentration of dust, moved northwestward towards the Béchar Province. Subsequently, the lifted dust mixed into the growing daytime planetary boundary layer (PBL) after sunrise and was then followed by the southerly/southeasterly wind which advected the dust poleward to the IP. At ~01 UTC on 21 February, the dust plume from the first dust storm had already reached the southern IP at that time (Figure 6d). The second dust plume crossed over the Atlas range at ~15 UTC on 21 February (Figure 3 in Part I). We investigate the mesoscale processes that organized both dust plumes next.

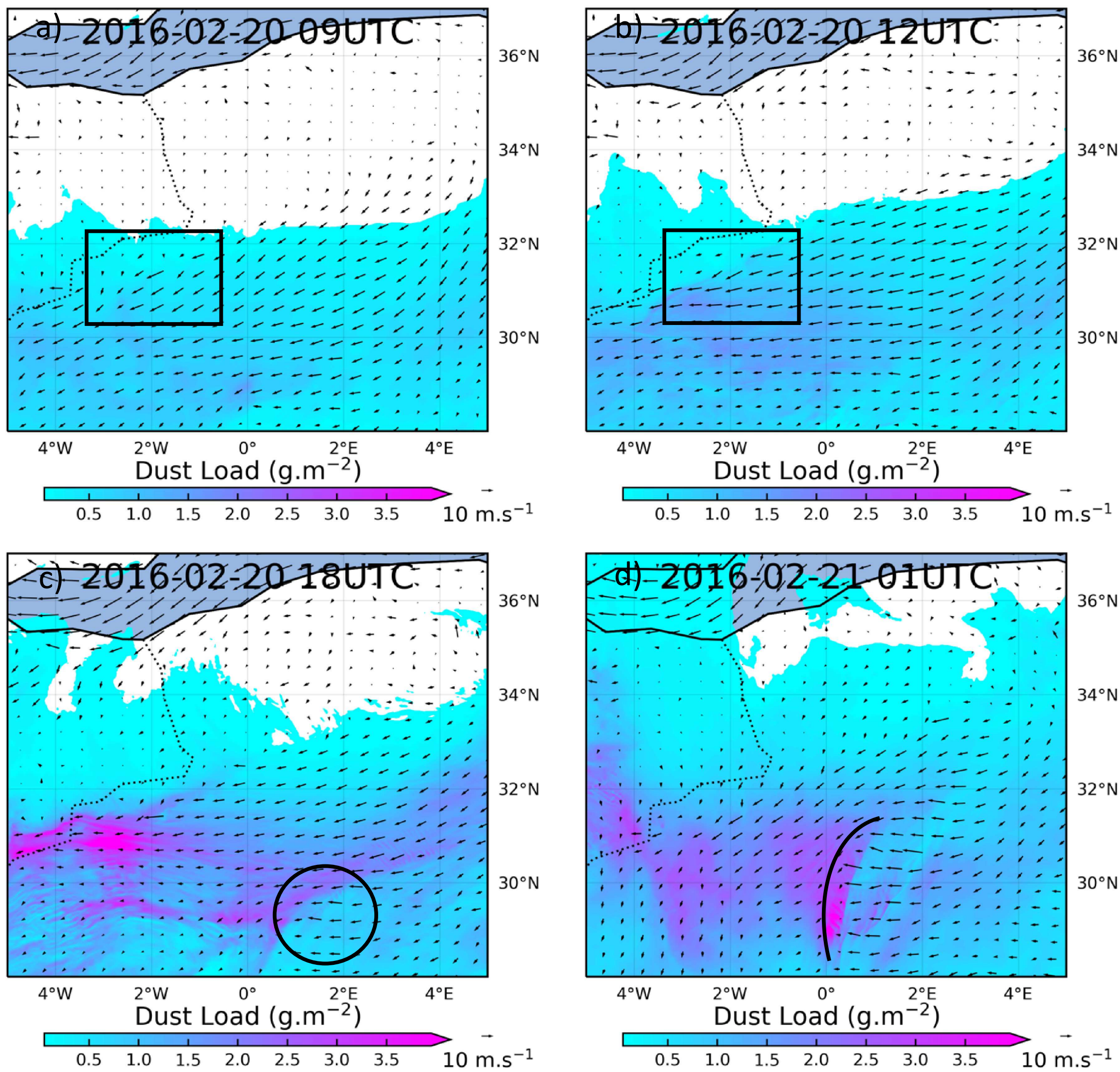

Figure 6: WRF-chem simulated 10m wind vector (m.s^{-1}) and dust load (fill in g.m^{-2}) at (a) 09 UTC, (b) 12 UTC, (c) 20 UTC on 20 and (d) 01 UTC on 21 February 2016. The black boxes in Figures c and d represent the Bechar Province region. The black circle in Figure c marks the region of increasing 10m wind. The black line in Figure d marks the second dust front.

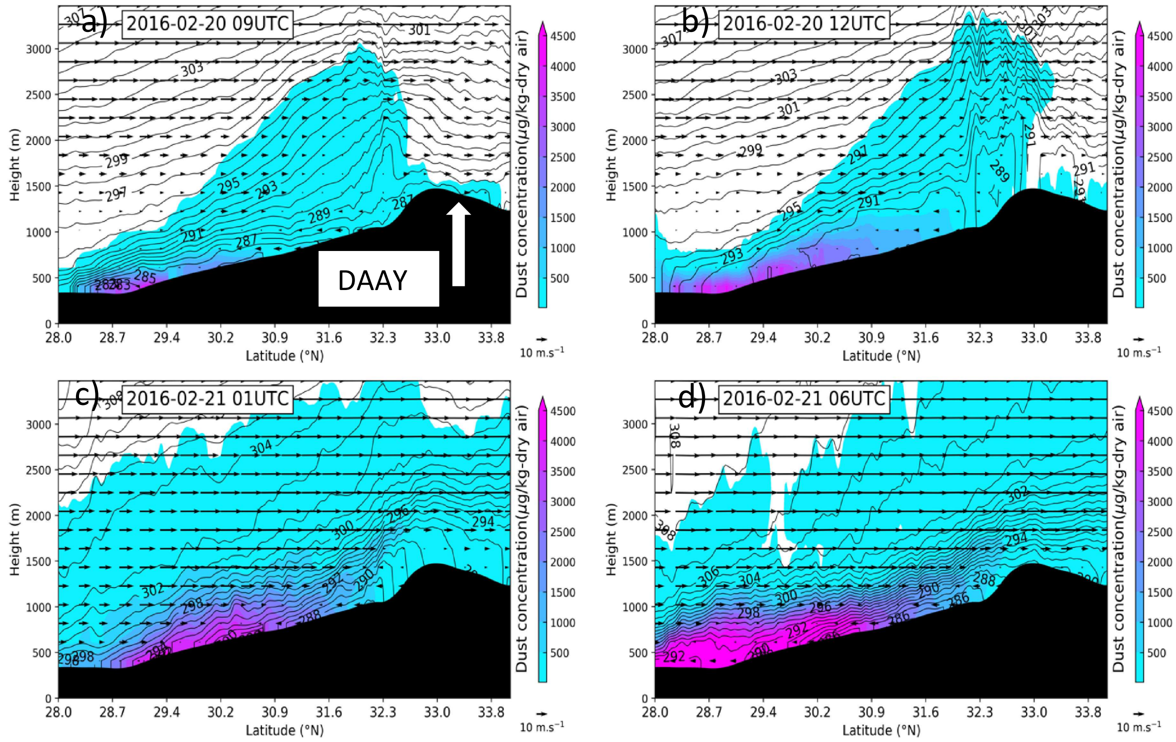

Figure 7: North-South transect at 0.28°W. Shown are WRF-Chem results for the vertical cross-section of potential temperature (K), wind vector (v and w, m.s^{-1}), and dust concentration (fill in µg.kg^{-1}) at the line E-F at (a) 09 UTC and (b) 12 UTC on 20 February 2016, and (c) 01 UTC and (d) 06 UTC on 21 February 2016. Location of transect is marked in Fig. 5a. White arrow mark the locations of stations

4.3 Meso-β/meso-γ-scale dynamics

The simulation results showed that the first dust storm was associated with BJ formation on the southeastern foothills of the SAM. The second dust storm was linked to the evolution of a long-lived westward propagating MGW near the northern edge of the Tinrhert Plateau in eastern Algeria and multiple hydraulic jumps on the western side of the TP (locations in Figure 2a). We discuss the formation of BJ, MGW, and multiple hydraulic jumps in this section. To this end, we use the vertical cross-sections of the simulated wind, potential temperature, and dust concentration.

4.3.1 Barrier Jet

Prior to the formation of the BJ, at 08 UTC on 20 February, the vertical cross-section along the line A-B shows a near-surface stable layer at 30-32°N (Figure 8a), consistent with the radiosonde at Béchar (Figure 4a). One can notice the near-surface stable layer with an easterly wind and vertically veering flow in the observed sounding. The inversion is ~350 m deep and the wind speed exceeds 18 m.s^{-1} at some locations already (Figure 8a), which is strong enough for emitting dust aerosols in source regions. The existence of a low-level stable layer is a critical prerequisite for BJ formation. An hour later, at 09 UTC, the near-surface wind speed along the line C-D between 30°N, 3°W and 33°N, 3.3°E largely exceeded 14 m.s^{-1} with a maxima >22 m.s^{-}

$^{-1}$ at ~30.6°N, 2°W around 750 m above sea level (ASL) (marked by circle in Figure 8b). This wind speed maximum is the center of the BJ.

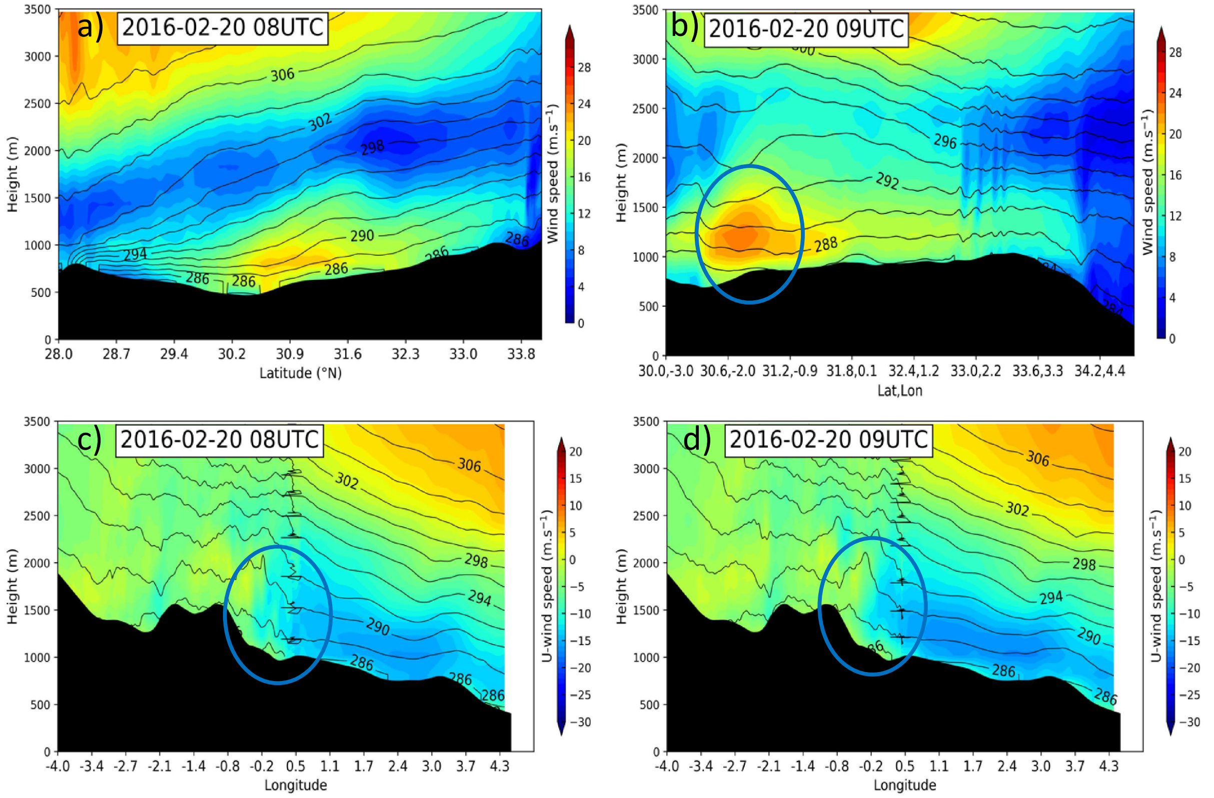

Figure 8: Horizontal winds and potential temperature transects for the first dust storm. Shown are simulation results for the vertical cross-sections of potential temperature (lines in K) and wind speed (fill in m.s^{-1}) at (a) 08 UTC along the line A-B and (b) 09 UTC along the line C-D on 20 February 2016. Vertical cross-section of potential temperature and u-wind speed along the line G-H at (c) 08 UTC and (d) at 09 UTC on 20 February 2016. Location of the transects are marked in Fig. 5a. The circle in Figure b marks the BJ, in c and d the flow blocking.

The typical low-level flow blocking required for BJ formation is seen in the cross-sections along the line G-H in Figures 8c-d (locations in Figure 5a). At 08 UTC, the time before a clear signature of the BJ, the low-level flow blocking is seen around 32.38°N, 0.5°W as indicated by the horizontal gradient in the zonal wind speed (marked by circles in Figures 8c-d). Here, the low Fr (=0.29) indicates insufficient kinetic energy of the air parcel to cross the SAM steep terrain. At 09 UTC, the Fr was ~0.27 at the same location, and the upstream flow remained in the subcritical flow regime between 08-09 UTC. During this period, the blocked flow accelerated parallel to the mountain barrier forming the BJ. The BJ formation is further supported by the highly baroclinic conditions exhibiting strong quasi-geostrophic warm air advection and veering vertical wind shear (Figures 1b, 1d, 1f, 4a and 5). All these characteristics are typical for a BJ.

4.3.2 Mesoscale gravity wave

At ~08 UTC on 20 February, a long-lived westward propagating MGW was triggered near the northern edge of the Tinrhert Plateau in eastern Algeria at ~29°N, 9°E. The MGW reached the western part of the TP by 15 UTC on the same day. The details of the MGW mechanisms are discussed in section 4.4. At 18 UTC on 20 February, when the westward propagating MGW crossed the TP, a signal of a hydraulic jump appeared on its lee side. The sinking and overturning low-level isentropic surfaces at ~1.5-2.1°E mark this hydraulic jump (circle in Figure 9a). The near-surface wind decreased downstream of the jump, while the vertical wind shear is large in the jump region (circle in Figure 9c). The strong change of Fr from 0.4 immediately downstream of the jump region at ~1.2°E to 1.67 immediately upstream at ~1.3°E further supports the existence of the hydraulic jump. At 01 UTC on 21 February, there were multiple regions of sub- and supercritical regimes as indicated by sinking and bulging isentropes accompanying multiple differences in wind speed on the western slope of the TP at ~0-1.5°E (circles in Figures 9b and 9d). The situation was further characterized by strong ascent at the leading edge of the jump ~0.2°E indicated by the vertical orientation of the isentropes and large turbulent kinetic energy (TKE) associated with the jump (circles in Figures 9b-f). These features point to the occurrence of multiple hydraulic jumps on the western side of the TP leading to a nocturnal increase in near-surface dust concentrations (Figures 9g-h).

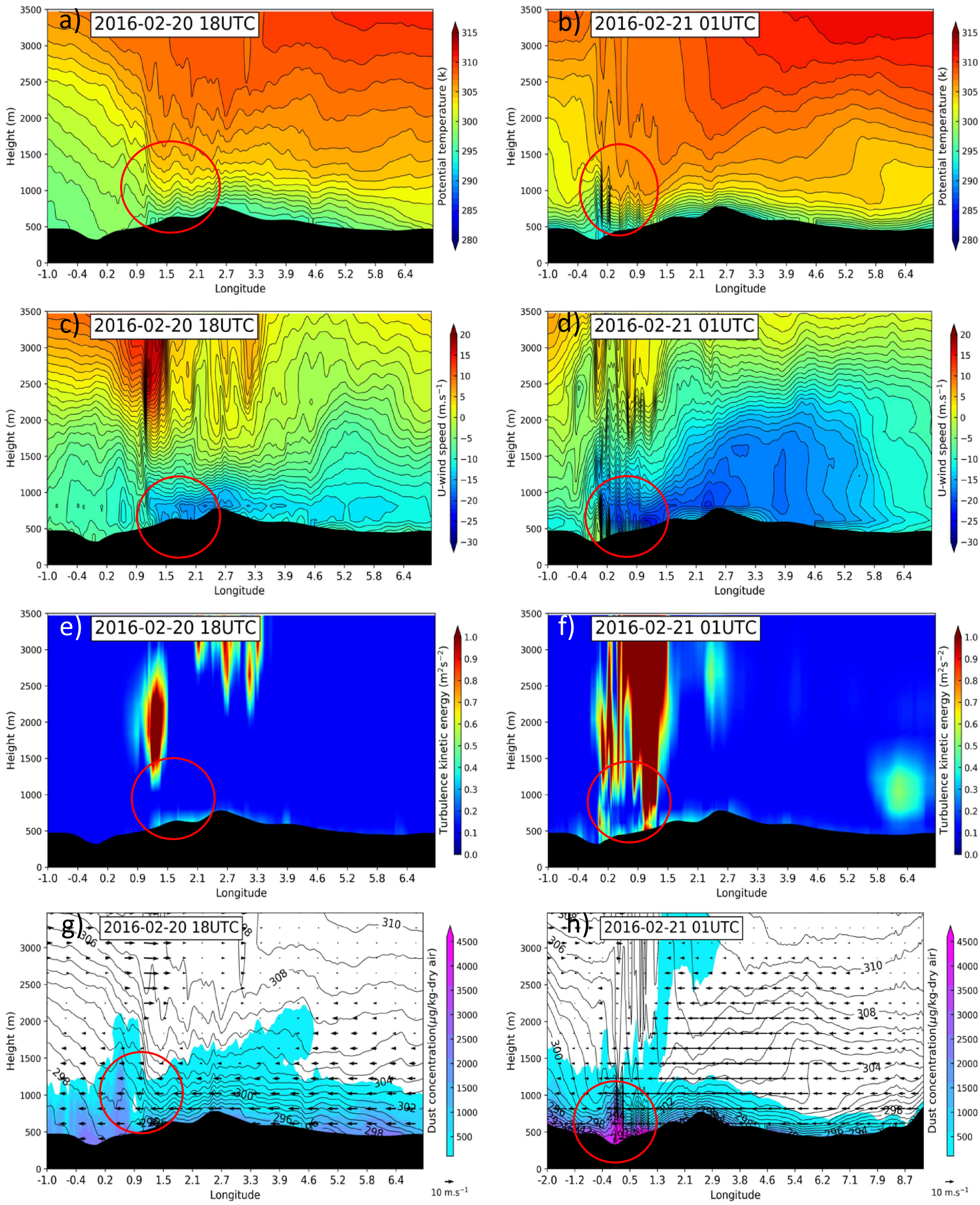

Figure 9: East-West transect at 29°N for the second dust storm. Shown are WRF-Chem results for the vertical cross-sections at 18 UTC on 20 February (left column) and 01 UTC on 21 February (right column) for (a, b) potential temperature, (c, d) u-wind component, (e, f) PBL TKE (fill in $m^2.s^{-2}$), and (g, h) potential temperature (line in K), wind vector (u, w) and dust

concentration. The circle marks the region of the hydraulic jump, increasing wind, and dust concentration.

4.4 Mesoscale gravity wave generation and maintenance

To describe the MGW generation and its maintenance mechanism(s), we analyzed the vertical cross-sections of potential temperature, wind, and Brunt-Väisälä frequency along and extending well beyond the line I-J (Fig. 5a) from 2°W-9°E using the simulation output (Figure 10). The MGW was triggered at ~08 UTC on 20 February when cool air descended into the stably stratified air over the lower terrain of the Tinrhert Plateau in eastern Algeria (circle in Figure 10a). The undulating isentropes, together with an ascent-descent pattern at ~5-9°E mostly in quadrature, indicates the existence of a gravity wave (GW, e.g., Uccellini and Koch, 1987). Two hours later, at 10 UTC, the GW propagated continuously westward with a phase speed of ~10.7 m.s^{-1} (Figure 10b). Atmospheric GWs are highly dispersive in nature and propagate vertically rapidly losing energy which may limit their long-range horizontal propagation from a source region. However, a long-lived MGW like the one that develops here, travels across long distances away from its source region upon satisfying conditions that maintains the wave's energy (Lin, Y., 2007). The wave maintenance conditions in our case follow Lindzen and Tung (1976). They described three key features that are evident for the MGW assessed here as follows: (1) the existence of a near-surface stably stratified layer, indicated by closed isentropes and a high Brunt-Väisälä frequency N (Figures 10a-d), (2) low-level easterly wind, westerly wind aloft, and a mixed layer in between (Figures 10e-f) facilitating a critical layer above the ducting layer near 1800 m, (3) the vertical cross-section of Brunt-Väisälä frequency and wind shear (Figures 10a-d) indicating the low Richardson number Ri ~0.175 (N = ~0.15 s^{-1}, dU = ~5 m.s^{-1}, and dz = ~1400) above the duct within the critical layer. The presence of the surface inversion, the critical layer above the duct within the phase reversal velocity at a low and an upper-level, and the Ri<0.25 within that critical layer are consistent with the Lindzen and Tung (1976) criteria for ducting/maintenance. The GW was therefore trapped beneath ~2 km and traveled downwind for a longer duration, i.e., several hundred km and several hours, such that it reached the mesoscale distance and period criterion.

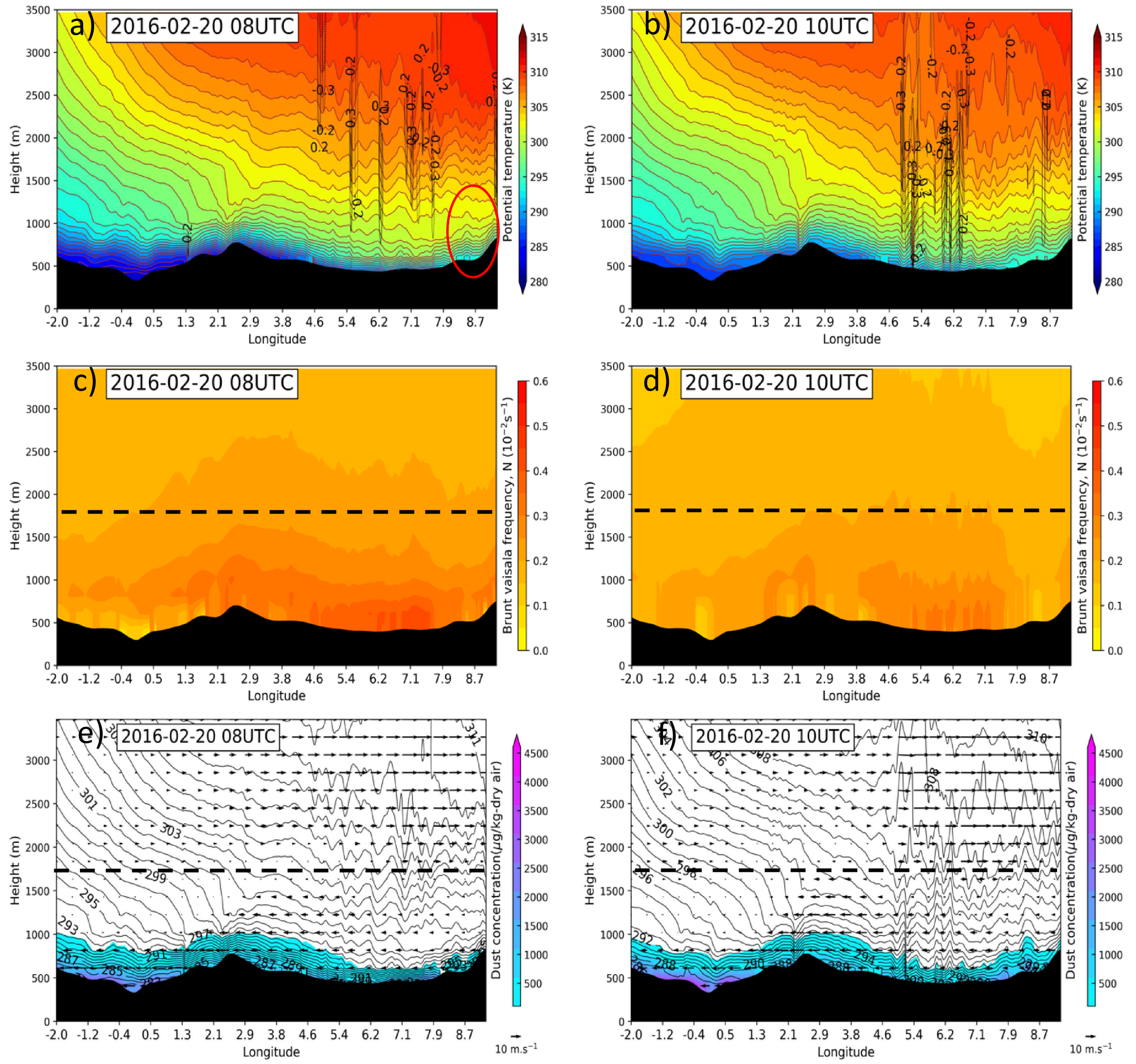

Figure 10: East-West transect at 29°N for the second dust storm. Shown are WRF-Chem results for the vertical cross-sections at 08 UTC (left column) and 10 UTC (right column) on 20 February 2016 for (a, b) potential temperature and w wind (solid line for positive w and dashed lined for negative w in $m.s^{-1}$), (c, d) Brunt-Väisälä frequency (N, shaded in s^{-1}), (e, f) potential temperature (line in K), wind vector (u, w) and dust concentration. The dashed line at ~1.8 km represents the wave critical level above the duct.

Further evidence for the MGW is the relationship between the spatial distribution of the near-surface pressure perturbation (p') and the wind perturbation (u'). In a ducted gravity wave, the spatial distribution of p' and u' are positively correlated (e.g., Koch and Golus, 1988; Coleman and Knupp, 2009). Subsidence warming ahead of a wave trough results in a p' minimum, while adiabatic cooling results in a p' maximum in the wave ridge (Coleman and Knupp, 2009). Consistent with the literature, at 10 UTC on 20 February, a positive correlation between p' and u' was found along the 29°N transect (Figure 11b), illustrating the spatial extent of the westward propagating MGW. Noticeable is the evolving high-low alternating pattern of p' and u', consistent with the pattern of up- and downward motion (Figures 11a-b). The schematic depiction of the relationship between p' and u' (Figure 11c) indicates that when p' and u' are in phase, the maximum vertical upward (downward) motion occurs near the nodal point before the wave ridge (trough). Such a sustained and high amplitude MGW triggers strong near-surface winds that result in dust emission during its course of motion in a region of several hundred kilometers.

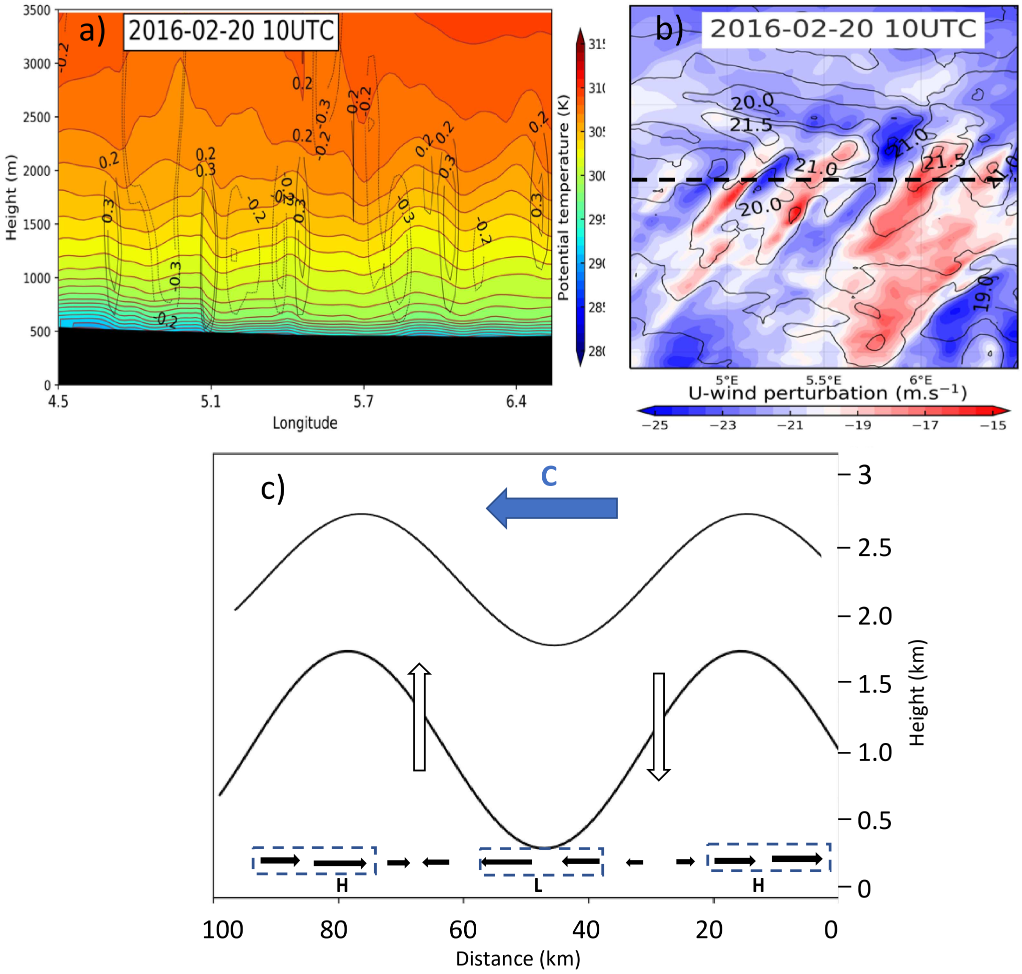

Figure 11: MGW during the second dust storm. Shown are the (a) WRF-Chem simulated vertical cross-section of potential temperature and vertical wind (solid line for positive w and dashed lined for negative w in m.s^{-1}) along 29°N at 10 UTC on 20 February 2016, (b) simulated perturbations in the zonal wind (u', shading) and pressure (p', contours in hPa) at the lowest model level at 10 UTC on 20 February 2016. The dashed black line in b marks the position of the transect at 29°N shown in a. (c) Schematic diagram to show p' and u' associated with a ducted gravity wave. The solid black lines represent isentropes, H and L indicate the regions of maximum and minimum pressure perturbations, horizontal black arrows indicate the perturbation of the wind vector (maximum and minimum near H and L, respectively), white arrows indicate the vertical motions, blue arrow indicates the wave propagation direction with the phase velocity (C ~10.7 m.s^{-1}).

4.5 Vertical distribution and poleward transport of lifted dust

The vertical distribution and poleward transport of dust to the IP were analyzed using the simulated vertical cross-sections of potential temperature, wind, dust concentrations, and 700 hPa horizontal winds. At ~09 UTC on 20 February, the emitted dust aerosols from the first dust storm was mostly confined to the near-surface stable layer with a minimal amount reaching 2 km ASL (Figure 7a). The weak southerly wind near ~2 km did not advect a substantial amount of dust poleward. This situation changed with the growing daytime PBL. At 12 UTC, a significant amount of dust was mixed into the deeper convective PBL, reaching altitudes >2.5 km (Figure 7b). This dust plume was subsequently advected poleward, which can be proven by the poleward advection of the simulated dust plume and the observed reduction in visibility at the DAAY station (Figures 2f and 7b).

The concentrated dust layer from the second dust storm was mostly confined to altitudes <800 m at the foothills of the SAM at 01 UTC on 21 February (Figure 7c). During the following morning, at 06 UTC, the dust layer expanded vertically and reached >2.5 km (Figure 7d). The predominant southerly/southeasterly mid-tropospheric flow advected the available dust poleward and crossed the SAM by midday.

5. Summary and conclusions

This study investigated the meso-β/meso-γ-scale dynamical processes responsible for the development of the two consecutive severe dust storms over the southeastern part of the SAM during 20-21 February 2016 that impacted the entire IP. The key meteorological findings that organized these dust storms include (1) the evolution of the BJ on the southeastern foothills of the SAM and (2) the development of multiple hydraulic jumps associated with an MGW on the southern flank of the TP. To the best of our knowledge, this study is the first to document the role of a BJ and multiple hydraulic jumps associated with a long-lived MGW in organizing a severe dust outbreak from Northwest Africa towards Europe.

Figure 12 shows the schematic depiction of the key mesoscale meteorological dynamics involved in this dust outbreak that had two phases. In Phase I, an easterly/north-northeasterly low-level Mediterranean flow was blocked by the SAM and resulted in BJ on its southeastern foothills. The strong wind associated with the intensification of the BJ after sunrise emitted a massive amount of dust on 20 February 2016 and formed the first dust plume. In Phase II, the MGW affected the western flank of the Tinrhert Plateau in eastern Algeria during the morning of 20 February 2016. The MGW triggered multiple hydraulic jumps on the western flank of the TP. The strengthening downslope wind and TKE accompanying the hydraulic jumps enhanced the dust emission on the lee side of the TP and resulted in the second dust plume on 21 February 2016. The lifted dust extended over 2-3 km in altitude due to increasing convective turbulence in the growing daytime PBL. The predominantly southerly/southeasterly mid-tropospheric flow subsequently advected the dust plume poleward to the IP.

This work underlines the importance of high-resolution numerical modeling in dust storm analyses and operational dust forecasting. The high-resolution model can resolve topographically induced dust-emitting peak winds like the BJ and hydraulic jumps, which are difficult to represent in coarse-resolution (aerosol-) climate and weather prediction models and are rarely observed in the virtually nonexistent meteorological instrumentation in this data sparse unpopulated region. It should be noted here that each dust storm has a unique characteristic concerning the dynamics associated with the dust emission and transport processes. However, to better quantify the atmospheric dust loading in a longer time span, the impact of climate change and biological activities over the complex terrain on land cover change need to be addressed along with other multi-scale dynamical mechanisms critical for dust emission and subsequent transport processes.

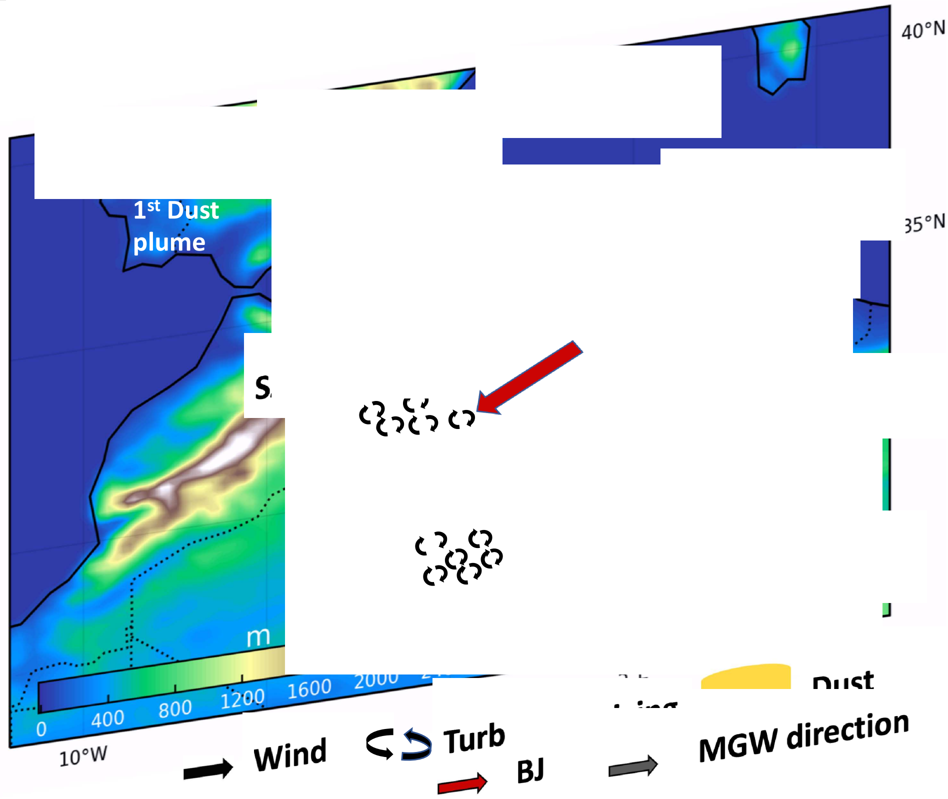

Figure 12: Schematic depiction of the time and location of the BJ and hydraulic jumps associated with MGW and subsequent transport of dust to the IP. Red arrow represents the BJ and gray arrow represents the MGW propagation direction.

Acknowledgments

Partial support from the Spanish Ministry of Economy and Competitiveness and the European Regional Development Funding, under grant CGL2015-70741-R (FRESA Project), is acknowledged. We thank the National Center for Atmospheric Research (NCAR) Computational and Information System Laboratory and the National Science Foundation (NSF) for providing the high-performance computing support from the Cheyenne (doi:10.5065/D6RX99HX) to perform high-resolution WRF-Chem simulations. We also express thanks to the various institutions for providing the following datasets: (1) the IOWA State University for the METAR dataset, (2) the NASA for providing MODIS aerosol optical depth dataset, (3) the ECMWF for the ERA-Interim reanalysis dataset, and (4) the University of Wyoming for sounding data.

References:

Bell, G. D., & L. F. Bosart (1988): Appalachian cold-air damming. Mon. Weather Rev., 116, 137–161. https://doi.org/10.1175/1520-0493(1988)116<0137:ACAD>2.0.CO;2.

Braun, S. A., R. A. Houze Jr., & B. F. Smull (1997): Airborne dual-Doppler observations of an intense frontal system approaching the Pacific Northwest coast. Mon. Weather Rev., 125, 3131–3156. https://doi.org/10.1175/1520-0493(1997)125<3131:ADDOOA>2.0.CO;2.

Chen, F., & Dudhia, J. (2001). Coupling and advanced land surface-hydrology model with the Penn State-NCAR MM5 modeling system. Part I: Model implementation and sensitivity. Mon. Weather Rev., 129(4), 569–585. https://doi.org/10.1175/1520-0493(2001)129<0569:CAALSH>2.0.CO;2.

Clarke, R. H. (1972): The morning glory: An atmospheric hydraulic jump. J. Appl. Meteor., 11, 304–311. https://doi.org/10.1175/1520-0450(1972)011<0304:TMGAAH>2.0.CO;2.

Coleman, T. A., & Knupp, K. R. (2009). Factors affecting surface wind speeds in gravity waves and wake lows. Wea. Forecasting, *24*(6), 1664–1679. https://doi.org/10.1175/2009WAF2222248.1.

Colle, B. A., C. F. Mass, K. A. Loescher, G. S. Young, & N. S. Winstead (2006): Climatology of barrier jets along the Alaskan coast. Part II: Large-scale and sounding composites. Mon. Weather Rev., 134, 454–477. https://doi.org/10.1175/MWR3038.1.

Cox, J. A. W., Steenburgh, W. J., Kingsmill, D. E., Shafer, J. C., Colle, B. A., Bousquet, O., et al. (2005). The kinematic structure of a Wasatch Mountain winter storm during IPEX IOP3. Mon. Weather Rev. (Vol. 133). https://doi.org/10.1175/MWR-2875.1.

Dee, D.P., et al. (2011). The ERA-Interim reanalysis: Configuration and performance of the data assimilation system. Q. J. R. Meteorol. Soc., 137, 553–597. https://doi.org/10.1002/qj.828.

Dhital, S., Kaplan, M. L., Orza, J. A. G., & Fiedler, S. (2020). Atmospheric dynamics of a Saharan dust outbreak over Mindelo, Cape Verde Islands, preceded by Rossby wave breaking: Multiscale observational analyses and simulations. J. Geophys. Res.: Atmosphere, 125, e2020JD032975. https://doi.org/10.1029/2020JD032975.

Dudhia, J. (1989). Numerical study of convection observed during the Winter Monsoon Experiment using a mesoscale two-dimensional model. J. Atmos. Sci., 46(20), 3077-3107. https://doi.org/10.1175/1520-0469(1989)046<3077:NSOCOD>2.0.CO;2.

Ek, M. B., Mitchell, K. E., Lin, Y., Rogers, E., Grunmann, P., Koren, V., et al. (2003). Implementation of Noah land surface model advances in the National Centers for Environmental Prediction operational mesoscale Eta model. J. Geophys. Res.: Atmosphere, 108(D22), 8851. https://doi.org/10.1029/2002JD003296.

Gama, C., Ribeiro, I., Lange, A. C., Vogel, A., Ascenso, A., Seixas, V., et al. (2019). Performance assessment of CHIMERE and EURAD-IM' dust modules. Atmo. Pollut. Res., 10(4), 1336–1346. https://doi.org/10.1016/j.apr.2019.03.005.

Ginoux, P., Chin, M., Tegen, I., Prospero, J. M., Holben, B., Dubovik, O., & Lin, S.-J. (2001). Sources and distributions of dust aerosols simulated with the GOCART model. J. Geophys. Res.: Atmosphere, 106(D17), 20255–20273. https://doi.org/10.1029/2000JD000053.

Gläser, G., Knippertz, P., & Heinold, B. (2012). Orographic effects and evaporative cooling along a subtropical cold front: The case of the spectacular saharan dust outbreak of March

2004. Mon. Weather Rev., 140(8), 2520–2533. https://doi.org/10.1175/MWR-D-11-00315.1.

Grell, G. A., Peckham, S. E., Schmitz, R., McKeen, S. A., Frost, G., Skamarock, W. C., & Eder, B. (2005). Fully coupled “online” chemistry within the WRF model. Atmos. Environ., 39(37), 6957–6975. https://doi.org/10.1016/j.atmosenv.2005.04.027.

Janjic, Z. (2002). Nonsingular Implementation of the Mellor-Yamada Level 2.5 Scheme in the NCEP Meso model. NCEP Office Note 437, pp 61.

Janjic, Z. I. (1994). The step-mountain eta coordinate model: further developments of the convection, viscous sublayer, and turbulence closure schemes. Mon. Weather Rev., 122(5), 927–945. https://doi.org/10.1175/1520-0493(1994)122<0927:TSMECM>2.0.CO;2.

Kaplan, M. L., Koch, S. E., Lin, Y. L., Weglarz, R. P., & Rozumalski, R. A. (1997). Numerical simulations of a gravity wave event over CCOPE. Part I: The role of geostrophic adjustment in mesoscale jetlet formation. Mon. Weather Rev. (Vol. 125). https://doi.org/10.1175/1520-0493(1997)125<1185:NSOAGW>2.0.CO;2.

Kaplan, M. L., Vellore, R. K., Marzette, P. J., & Lewis, J. M. (2012). The role of windward-side diabatic heating in Sierra Nevada spillover precipitation. J. Hydrometeorol., 13(4), 1172–1194. https://doi.org/10.1175/JHM-D-11-06.1.

Karyampudi, V. M., Kaplan, M. L., Koch, S. E., & Zamora, R. J. (1995). The Influence of the Rocky Mountain on the 13–14 April 1986 Severe Weather Outbreak. Part I: Mesoscale Lee Cyclogenesis and Its Relationship to Severe Weather and Dust Storms. Mon. Weather Rev. https://doi.org/10.1175/1520-0493(1995)123<1394:tiotrm>2.0.co;2.

Ke, C. Y., Chung, K. S., Chen Wang, T. C., & Liou, Y. C. (2019). Analysis of heavy rainfall and barrier-jet evolution during Mei-Yu season using multiple Doppler radar retrievals: a case study on 11 June 2012. Tellus, Series A: Dyn. Meteorol. and Oceanogr., 71(1), 1–21. https://doi.org/10.1080/16000870.2019.1571369.

Knippertz, P., C. Deutscher, K. Kandler, T. Müller, O. Schulz, & L. Schütz (2007). Dust mobilization due to density currents in the Atlas region: Observations from the Saharan Mineral Dust Experiment 2006 field campaign, J. Geophys. Res., 112, D21109, doi:10.1029/2007JD008774.

Koch, S. E. & R. E. Golus (1988). A mesoscale gravity wave event observed during CCOPE. Part I: Multiscale statistical analysis of wave characteristics. Mon. Weather Rev., 116(12): 2527–2544. https://doi.org/10.1175/1520-0493(1988)116<2527:AMGWEO>2.0.CO;2.

Li, J., & Chen, Y. L. (1998). Barrier jets during TAMEX. Mon. Weather Rev. (Vol. 126). https://doi.org/10.1175/1520-0493(1998)126<0959:BJDT>2.0.CO;2.

Lin, Y. (2007). Mesoscale Dynamics. Cambridge: Cambridge University Press. doi:10.1017/CBO9780511619649.

Lindzen, R. S. & K. K. Tung (1976). Banded convective activity and ducted gravity waves. Mon. Weather Rev., 104 (12): 1602–1617. https://doi.org/10.1175/1520-0493(1976)104<1602:BCAADG>2.0.CO;2.

Loescher, K. A., Young, G. S., Colle, B. A., & Winstead, N. S. (2006). Climatology of barrier jets along the Alaskan Coast. Part I: Spatial and temporal distributions. Mon. Weather Rev. (Vol. 134). https://doi.org/10.1175/MWR3037.1.

Luna-Niño, R., & Cavazos, T. (2018). Formation of a coastal barrier jet in the Gulf of Mexico due to the interaction of cold fronts with the Sierra Madre Oriental mountain range. Q. J. Roy. Meteorol. Soc., 144(710), 115–128. https://doi.org/10.1002/qj.3188.

Mellor, G. L., & Yamada, T. (1974). A Hierarchy of Turbulence Closure Models for Planetary Boundary Layers. J. Atmos. Sci., 31(7), 1791–1806. https://doi.org/10.1175/1520-0469(1974)031<1791:ahotcm>2.0.co;2.

Mlawer, E. J., Taubman, S. J., Brown, P. D., Iacono, M. J., & Clough, S. A. (1997). Radiative transfer for inhomogeneous atmospheres: RRTM, a validated correlated-k model for the longwave. J. Geophys. Res.: Atmosphere, 102(14), 16663–16682. https://doi.org/10.1029/97jd00237.

Neiman, P. J., Hughes, M., Moore, B. J., Martin Ralph, F., & Sukovich, E. M. (2013). Sierra barrier jets, atmospheric rivers, and precipitation characteristics in northern California: A composite perspective based on a network of wind profilers. Mon. Weather Rev., 141(12), 4211–4233. https://doi.org/10.1175/MWR-D-13-00112.1.

Neiman, P. J., Sukovich, E. M., Martin Ralph, F., & Hughes, M. (2010). A seven-year wind profiler-based climatology of the windward barrier jet along California's Northern Sierra Nevada. Mon. Weather Rev., 138(4), 1206–1233. https://doi.org/10.1175/2009MWR3170.1.

Orza, J. A. G., Dhital, S., Fiedler, S., & Kaplan, M. L. (2020). Large scale upper-level precursors for dust storm formation over North Africa and poleward transport to the Iberian Peninsula. Part I: An observational analysis. Atmos. Environ., 237, 117688. https://doi.org/10.1016/j.atmosenv.2020.117688.

Parish, T. R. (1982): Barrier winds along the Sierra Nevada mountains. J. Appl. Meteor., 21, 925–930. https://doi.org/10.1175/1520-0450(1982)021<0925:BWATSN>2.0.CO;2

Pokharel, A. K., Kaplan, M. L., & Fiedler, S. (2017). Subtropical Dust Storms and Downslope Wind Events. J. Geophys. Res.: Atmosphere, 122(19), 10191–10205. https://doi.org/10.1002/2017JD026942.

Roberts, A. J., & Knippertz, P. (2014). The formation of a large summertime saharan dust plume: Convective and synoptic-scale analysis. J. Geophys. Res., 119(4), 1766–1785. https://doi.org/10.1002/2013JD020667.

Ruppert, J. H., & Bosart, L. F. (2014). A case study of the interaction of a mesoscale gravity wave with a mesoscale convective system. Mon. Weather Rev., 142(4), 1403–1429. https://doi.org/10.1175/MWR-D-13-00274.1

Thompson, G., Field, P. R., Rasmussen, R. M., & Hall, W. D. (2008). Explicit forecasts of winter precipitation using an improved bulk microphysics scheme. Part II: Implementation of a new snow parameterization. Mon. Weather Rev., 136(12), 5095–5115. https://doi.org/10.1175/2008MWR2387.1.

Titos, G., Ealo, M., Pandolfi, M., Pérez, N., Sola, Y., Sicard, M., et al. (2017). Spatiotemporal evolution of a severe winter dust event in the western Mediterranean: Aerosol optical and physical properties. J. Geophys. Res.: Atmospheres, 122(7), 4052–4069. https://doi.org/10.1002/2016JD026252.

Uccellini, L. W., & S. E. Koch (1987): The synoptic setting and possible energy sources for mesoscale wave disturbances. Mon. Weather Rev., 115, 721–729. https://doi.org/10.1175/1520-0493(1987)115<0721:TSSAPE>2.0.CO;2.